On the development of an implicit high-order Discontinuous Galerkin method for DNS and implicit LES of turbulent flows

On the development of an implicit high-order Discontinuous Galerkin method for DNS and implicit LES of turbulent flows

F. Bassi, L. Botti, A. Colombo, A. Crivellini, A. Ghidoni, F. Massa

Original publication available at:

https://doi.org/10.1016/j.euromechflu.2015.08.010

On the development of an implicit high-order Discontinuous Galerkin method for DNS and implicit LES of turbulent flows

F. Bassi[a], L. Botti[a], A. Colombo[a,*], A. Crivellini[b], A. Ghidoni[c], F. Massa[a]

[a] *Università degli Studi di Bergamo, Dipartimento di Ingegneria e Scienze Applicate, Italy*
[b] *Università Politecnica delle Marche, Dipartimento di Ingegneria Industriale e Scienze Matematiche, Italy*
[c] *Università degli Studi di Brescia, Dipartimento di Ingegneria Meccanica e Industriale, Italy*

Abstract

In recent years Discontinuous Galerkin (DG) methods have emerged as one of the most promising high-order discretization techniques for CFD. DG methods have been successfully applied to the simulation of turbulent flows by solving the Reynolds averaged Navier–Stokes (RANS) equations with first-moment closures. More recently, due to their favourable dispersion and dissipation properties, DG discretizations have also been found very well suited for the Direct Numerical Simulation (DNS) and Implicit Large Eddy Simulation (ILES) of turbulent flows.

The growing interest in the implementation of DG methods for DNS and ILES is motivated by their attractive features. In particular, these methods can easily achieve high-order accuracy on arbitrarily shaped elements and are perfectly suited to *hp*-adaptation techniques. Moreover, their compact stencil is independent of the degree of polynomial approximation and is thus well suited for implicit time discretization and for massively parallel implementations.

In this paper we focus on recent developments and applications of an implicit high-order DG method for the DNS and ILES of both compressible and incompressible flows. High-order spatial and temporal accuracy has been achieved using the same numerical technology in both cases. Numerical inviscid flux formulations are based on the exact solution of Riemann problems (suitably perturbed in the incompressible case), and viscous flux discretizations rely on the BR2 scheme. Several types of high-order (up to order six) implicit schemes, suited also for DAEs, can be employed for accurate time integration. In particular, linearly implicit Rosenbrock-type Runge–Kutta schemes have been used for all the simulations presented in this work.

The massively separated incompressible flow past a sphere at $\mathrm{Re}_D = 1000$, with transition to turbulence in the wake region, is considered as a DNS test case, while the potential of the ILES is demonstrated by computing the compressible transitional flow at $\text{Re}_c = 60000$, $\text{M}_\infty = 0.1$ and $\alpha = 8°$, around the Selig-Donovan 7003 airfoil. The computed solutions are compared with experimental data and numerical results available in the literature, showing good agreement.

Keywords: Discontinuous Galerkin discretization, implicit high-order accurate time integration, linearly implicit Rosenbrock-type Runge-Kutta schemes, DNS, ILES, compressible and incompressible flows

1. Introduction

Research work on high-order Discontinuous Galerkin (DG) methods applied to CFD is still very active due to the features that make such methods quite attractive. In particular, DG methods can easily achieve high-order accuracy on arbitrarily shaped elements and are perfectly suited to *hp*-adaptation techniques. Moreover, the optimal compactness of DG discretization schemes is independent of the degree of polynomial approximation and is thus well suited for implicit time discretization and for massively parallel implementations of the schemes.

DG methods were already successfully applied to the simulation of compressible and incompressible turbulent flows, by solving the Reynolds averaged Navier–Stokes (RANS) equations with first-moment closures [1, 2, 3, 4, 5, 6, 7, 8, 9]. Thanks to their favourable dispersion and dissipation properties, DG methods were also found to be well suited for the Direct Numerical Simulation (DNS) and the Large Eddy Simulation (LES) of turbulent flows, [10, 11, 12, 13, 14, 15, 16]. More recently, investigating on the behaviour of DG methods applied to LES, several authors have found that such methods appear to have dissipation properties which are perfectly suited for an Implicit LES (ILES) of turbulent flows, *i.e.*, for a LES where the dissipation of the numerical scheme, behaving like a spectral cut-off filter, plays the role of subgrid-scale (SGS) models, like the Smagorinsky model, proper of “classical” LES approaches. This is the case of the works of Refs. [17, 15], where the authors analyse the accuracy of high-order DG methods for the coarse-

*Corresponding author: alessandro.colombo@unibg.it, Tel +39 0352052150, fax +39 0352052077

grid ("under-resolved") simulation of turbulent flows, and of Refs. [13, 16] where the authors explicitly refer to their approaches as ILES.

The aim of this work is to begin investigating the potential of a common computational framework, based on the DG method, to address the DNS and ILES of both compressible and incompressible turbulent flows. The governing equations are the Navier–Stokes equations, whereby the turbulent kinetic energy dissipation, at the appropriate spatial and temporal scales, should be provided by the numerical dissipation of the scheme. High-order spatial and temporal accuracy has been achieved using the same numerical technology for both compressible and incompressible flows. The numerical inviscid flux formulations are based on the exact solution of local Riemann problems, suitably perturbed in the incompressible case, see [18, 19], while the viscous flux discretizations rely on the BR2 scheme, see [20]. Several types of high-order (up to order six) implicit schemes can be used for the accurate time integration, *e.g.* Modified Extended BDF (MEBDF), Two Implicit Advanced Step-point (TIAS) [21, 22, 23], which allow to exploit the benefits of the high-order discretizations both in space and time. The performance of these schemes have been recently investigated, and, according to a preliminary analysis [24], the linearly implicit Rosenbrock-type Runge–Kutta schemes result as the most promising in terms of both accuracy and efficiency. The main attractive feature of this class of schemes is the need to solve only one linear system per stage for each time step, *i.e.*, the Jacobian matrix is assembled and factored only once. In this work we employ Rosenbrock-type schemes that preserve accuracy also when applied to systems of Differential Algebraic Equations (DAEs) as those arising from our discretization of the incompressible fluid dynamics governing equations.

The capabilities of the DG solver here presented are demonstrated by computing two well-known test cases: the DNS of the massively separated incompressible flow past a sphere at $\mathrm{Re}_D = 1000$, with transition to turbulence in the wake region, and the ILES of the transitional flow around the Selig-Donovan (SD) 7003 airfoil at $\mathrm{Re}_c = 60000$, $\mathrm{M}_\infty = 0.1$ and $\alpha = 8°$.

The simulation of transonic flows with shock-waves, where DG methods require to introduce some form of stabilization to control the numerical oscillation when flow discontinuities occur inside cells, *e.g.* [25], is beyond the scope of this paper.

The rest of the paper is organized as follows. A quick overview of the governing equations is given in Sec. 2, while Sec. 3 describes the space and time discretizations. Numerical results are discussed in Sec. 4 and conclusions are given in Sec. 5. Finally, Appendix A reports some notes on flow statistics computation in the context of an implicit modal DG framework.

2. Governing equations

Using Einstein notation, the Navier–Stokes equations for compressible flows read

$$\frac{\partial \rho}{\partial t} + \frac{\partial}{\partial x_j}(\rho u_j) = 0, \tag{1}$$

$$\frac{\partial}{\partial t}(\rho u_i) + \frac{\partial}{\partial x_j}(\rho u_j u_i) = -\frac{\partial p}{\partial x_i} + \frac{\partial \tau_{ji}}{\partial x_j}, \tag{2}$$

$$\frac{\partial}{\partial t}(\rho E) + \frac{\partial}{\partial x_j}(\rho u_j H) = \frac{\partial}{\partial x_j}\left[u_i \tau_{ij} - q_j\right], \tag{3}$$

where E and H are total energy and total enthalpy, respectively. The pressure, stress tensor and heat flux vector are given by

$$p = (\gamma - 1)\rho\left(E - u_k u_k/2\right), \tag{4}$$

$$\tau_{ij} = 2\mu\left[S_{ij} - \frac{1}{3}\frac{\partial u_k}{\partial x_k}\delta_{ij}\right], \tag{5}$$

$$q_j = -\frac{\mu}{\mathrm{Pr}}\frac{\partial h}{\partial x_j}, \tag{6}$$

where γ is the ratio of gas specific heats, S_{ij} is the mean strain-rate tensor

$$S_{ij} = \frac{1}{2}\left(\frac{\partial u_i}{\partial x_j} + \frac{\partial u_j}{\partial x_i}\right),$$

and Pr is the molecular Prandtl number.

For incompressible flows, we consider the set of governing equations

$$\frac{\partial u_j}{\partial x_j} = 0, \tag{7}$$

$$\frac{\partial u_i}{\partial t} + \frac{\partial}{\partial x_j}(u_j u_i) = -\frac{\partial p}{\partial x_i} + \frac{\partial \tau_{ji}}{\partial x_j}, \tag{8}$$

where the density has been assumed to be uniform and equal to one. The stress tensor τ_{ij} is again computed from Eq. (5), assuming a constant μ and keeping the velocity divergence in this equation.

3. Space and time discretization

3.1. The DG discrete setting

Let $\mathcal{T}_h = \{K\}$ denote a mesh of the domain $\Omega \in \mathbb{R}^d, d \in \{2, 3\}$ consisting of non-overlapping arbitrarily shaped elements K such that

$$\overline{\Omega}_h = \bigcup_{K \in \mathcal{T}_h} \overline{K}. \tag{9}$$

Following the idea to define discrete polynomial spaces in physical coordinates, see, *e.g.*, [20, 18, 26, 27, 28, 29], we consider DG approximations based on the space

$$\mathbb{P}^k_d(\mathcal{T}_h) \overset{\text{def}}{=} \left\{ v_h \in L^2(\Omega) \,|\, v_{h|K} \in \mathbb{P}^k_d(K),\ \forall K \in \mathcal{T}_h \right\}, \tag{10}$$

where k is a non-negative integer and $\mathbb{P}^k_d(K)$ denotes the restriction to K of the polynomial functions of d variables and total degree $\leq k$. To build a satisfactory basis for the space (10) we rely on the procedure presented in [30], see also [31, 32], allowing to obtain orthonormal and hierarchical basis functions by means of the modified Gram-Schmidt (MGS) algorithm. The starting set of basis functions for the MGS algorithm are the monomials defined over each elementary space $\mathbb{P}^k_d(K)$, $K \in \mathcal{T}_h$, in a reference frame relocated in the element barycenter and aligned with the principal axes of inertia of K. For the sake of presenting the DG discretization, we introduce the set $\mathcal{F}_h$ of the mesh faces $\mathcal{F}_h \stackrel{\text{def}}{=} \mathcal{F}_h^i \cup \mathcal{F}_h^b$, where $\mathcal{F}_h^b$ collects the faces located on the boundary of Ω_h and for any $F \in \mathcal{F}_h^i$ there exist two elements $K^+, K^- \in \mathcal{T}_h$ such that $F \in \partial K^+ \cap \partial K^-$. Moreover, for all $F \in \mathcal{F}_h^b$, $\mathbf{n}_F$ denotes the unit outward normal to Ω_h, whereas, for all $F \in \mathcal{F}_h^i$, $\mathbf{n}_F^-$ and $\mathbf{n}_F^+$ are the unit outward normals pointing to K^+ and K^-, respectively.

Since a function $v_h \in \mathbb{P}_d^k(\mathcal{T}_h)$ is double valued over an internal face $F \in \mathcal{F}_h^i$, we introduce the jump $[\![\cdot]\!]$ and average $\{\cdot\}$ trace operators, that is

$$[\![v_h]\!] \stackrel{\text{def}}{=} v_{h|K^+}\mathbf{n}_F^+ + v_{h|K^-}\mathbf{n}_F^-, \qquad \{v_h\} \stackrel{\text{def}}{=} \frac{v_{h|K^+} + v_{h|K^-}}{2}, \tag{11}$$

and consider them to act componentwise when applied to vector functions. Finally, the DG discretization of second-order viscous terms employs the lifting operators $\mathbf{r}_F$ and $\mathbf{r}$. For all $F \in \mathcal{F}_h$, we define the local lifting operator $\mathbf{r}_F : \left[L^2(F)\right]^d \rightarrow [\mathbb{P}_d^k(\mathcal{T}_h)]^d$, such that, for all $\mathbf{v} \in \left[L^2(F)\right]^d$,

$$\int_\Omega \mathbf{r}_F(\mathbf{v}) \cdot \boldsymbol{\tau}_h d\mathbf{x} = -\int_F \{\boldsymbol{\tau}_h\} \cdot \mathbf{v} dF \quad \forall \boldsymbol{\tau}_h \in [\mathbb{P}_d^k(\mathcal{T}_h)]^d. \tag{12}$$

The global lifting operator $\mathbf{r}$ is then defined as

$$\mathbf{r}(\mathbf{v}) \stackrel{\text{def}}{=} \sum_{F \in \mathcal{F}_h} \mathbf{r}_F(\mathbf{v}). \tag{13}$$

3.2. DG discretization of the Navier–Stokes equations

The Navier–Stokes equations for the m variables in d dimensions, Eqs. (1)-(2)-(3) or (7)-(8), can be written in compact form as

$$\mathbf{P}(\mathbf{w})\frac{\partial \mathbf{w}}{\partial t} + \nabla \cdot \mathbf{F}_c(\mathbf{w}) + \nabla \cdot \mathbf{F}_v(\mathbf{w}, \nabla \mathbf{w}) = \mathbf{0}, \tag{14}$$

where $\mathbf{w} \in \mathbb{R}^m$ is the unknown solution vector, $\mathbf{F}_c, \mathbf{F}_v \in \mathbb{R}^m \otimes \mathbb{R}^d$ are the inviscid and viscous flux functions, and $\mathbf{P}(\mathbf{w}) \in \mathbb{R}^m \otimes \mathbb{R}^m$ is a transformation matrix. Employing the conservative variables $\mathbf{w}_c = [\rho, \rho u_i, \rho E]^T$ for compressible flows and the primitive variables $\mathbf{w}_p = [p, u_i]^T$ for incompressible flows, $\mathbf{P}$ reduces to the identity matrix ($\mathbf{P} = \mathbf{I}$) in the former case and to the difference between the identity and a single-entry matrix ($\mathbf{P} = \mathbf{I} - \mathbf{J}^{11}$) in the latter.

Alternatives to the set $\mathbf{w}_c$ for compressible flows have been proposed by several authors for accuracy and robustness purposes. Primitive variables (p, u_i, T) are widely used for the preconditioning of the governing equations of low Mach number flows [33, 34, 35], and for the design of numerical schemes suited for both compressible and incompressible flows [36]. Such choice also simplifies the implementation of implicit contributions to the Jacobian matrix related to viscous terms and boundary conditions.

In this work, following the approach proposed by Bassi et al. in [37, 23], the positivity of the thermodynamic variables at a discrete level is ensured by employing a set of primitive variables where pressure and temperature have been replaced by their *logarithms*, $\widetilde{p} = \log(p)$ and $\widetilde{T} = \log(T)$. Essentially, we substitute in the governing equations the variables $(p,\ T)$ with $(e^{\widetilde{p}},\ e^{\widetilde{T}})$ and use a polynomial approximation for $\widetilde{p}$ and $\widetilde{T}$ in the DG discretization. Using then, for compressible flows, the set of variables $\mathbf{w} = [\widetilde{p}, u_i, \widetilde{T}]^T$, the transformation matrix $\mathbf{P}(\mathbf{w})$ reads

$$
\mathbf{P}(\mathbf{w}) = \begin{bmatrix} \rho_{\widetilde{p}} & 0 & 0 & 0 & \rho_{\widetilde{T}} \\ \rho_{\widetilde{p}} u_1 & \rho & 0 & 0 & \rho_{\widetilde{T}} u_1 \\ \rho_{\widetilde{p}} u_2 & 0 & \rho & 0 & \rho_{\widetilde{T}} u_2 \\ \rho_{\widetilde{p}} u_3 & 0 & 0 & \rho & \rho_{\widetilde{T}} u_3 \\ \rho_{\widetilde{p}} H + \rho h_{\widetilde{p}} - e^{\widetilde{p}} & \rho u_1 & \rho u_2 & \rho u_3 & \rho_{\widetilde{T}} H + \rho h_{\widetilde{T}} \end{bmatrix}, \tag{15}
$$

where

$$
\rho = e^{\left(\widetilde{p} - \widetilde{T}\right)}, \qquad \hat{e} = \frac{e^{\widetilde{T}}}{\gamma - 1}, \tag{16}
$$

$$
h_{\widetilde{p}} = \left.\frac{\partial h}{\partial \widetilde{p}}\right|_{\widetilde{T}} = \hat{e}_{\widetilde{p}} + \frac{e^{\widetilde{p}}}{\rho} - \frac{\rho_{\widetilde{p}}}{\rho^2} e^{\widetilde{p}}, \qquad h_{\widetilde{T}} = \left.\frac{\partial h}{\partial \widetilde{T}}\right|_{\widetilde{p}} = \hat{e}_{\widetilde{T}} - \frac{\rho_{\widetilde{T}}}{\rho^2} e^{\widetilde{p}}, \tag{17}
$$

and assuming an ideal gas

$$
\rho_{\widetilde{p}} = \left.\frac{\partial \rho}{\partial \widetilde{p}}\right|_{\widetilde{T}} = \rho, \qquad \rho_{\widetilde{T}} = \left.\frac{\partial \rho}{\partial \widetilde{T}}\right|_{\widetilde{p}} = -\rho, \tag{18}
$$

$$\hat{e}_{\widetilde{p}} = \left.\frac{\partial \hat{e}}{\partial \widetilde{p}}\right|_{\widetilde{T}} = 0, \qquad \hat{e}_{\widetilde{T}} = \left.\frac{\partial \hat{e}}{\partial \widetilde{T}}\right|_{\widetilde{p}} = \hat{e}, \tag{19}$$

$$h_{\widetilde{p}} = 0, \qquad h_{\widetilde{T}} = \hat{e}_{\widetilde{T}} - \frac{e^{\widetilde{p}}}{\rho}. \tag{20}$$

By multiplying Eq. (14) by an arbitrary smooth test function $\mathbf{v} = \{v_1, \ldots, v_m\}$, and integrating by parts, we obtain the weak formulation

$$\int_{\Omega} \mathbf{v} \cdot \left(\mathbf{P}\left(\mathbf{w}\right) \frac{\partial \mathbf{w}}{\partial t}\right) d\mathbf{x} - \int_{\Omega} \nabla \mathbf{v} : \mathbf{F}\left(\mathbf{w}, \nabla \mathbf{w}\right) d\mathbf{x} + \int_{\partial\Omega} \mathbf{v} \otimes \mathbf{n} : \mathbf{F}\left(\mathbf{w}, \nabla \mathbf{w}\right) d\sigma = \mathbf{0}, \tag{21}$$

where $\mathbf{F}$ is the sum of the inviscid and viscous flux functions and $\mathbf{n}$ is the unit vector normal to the boundary.

To discretize Eq. (21) we replace the solution $\mathbf{w}$ and the test function $\mathbf{v}$ with a finite element approximation $\mathbf{w}_h$ and a discrete test function $\mathbf{v}_h$, respectively, where $\mathbf{w}_h$ and $\mathbf{v}_h$ belong to the space $\mathbf{V}_h \stackrel{\text{def}}{=} [\mathbb{P}^k_d(\mathcal{T}_h)]^m$. For each of the m equations of system (21), and without loss of generality, we choose the set of test and shape functions in any element K coincident with the set $\{\phi\}$ of N^K_{dof} orthogonal and hierarchical basis functions in that element. With this choice each component $w_{h,j}$, $j = 1, \ldots, m$, of $\mathbf{w}_h \in \mathbf{V}_h$ can be expressed, in terms of the elements of the global vector $\mathbf{W}$ of unknown degrees of freedom, as $w_{h,j} = \phi_l W_{j,l}$, $l = 1, \ldots, N^K_{dof}$, $\forall K \in \mathcal{T}_h$. Then, the DG discretization of the Navier–Stokes equations consists in seeking, for $j = 1, \ldots, m$, the elements of $\mathbf{W}$ such that

$$\begin{aligned} \sum_{K \in \mathcal{T}_h} \int_K \phi_i P_{j,k}\left(\mathbf{w}_h\right) \phi_l \frac{dW_{k,l}}{dt} d\mathbf{x} - \sum_{K \in \mathcal{T}_h} \int_K \frac{\partial \phi_i}{\partial x_n} F_{j,n}\left(\mathbf{w}_h, \nabla_h \mathbf{w}_h + \mathbf{r}\left([\![\mathbf{w}_h]\!]\right)\right) d\mathbf{x} \\ + \sum_{F \in \mathcal{F}_h} \int_F [\![\phi_i]\!]_n \widehat{F}_{j,n}\left(\mathbf{w}_h^{\pm}, \left(\nabla_h \mathbf{w}_h + \eta_F \mathbf{r}_F\left([\![\mathbf{w}_h]\!]\right)\right)^{\pm}\right) d\sigma = 0, \end{aligned} \tag{22}$$

for $i = 1, \ldots, N^K_{dof}$. In Eq. (22) repeated indices imply summation over the ranges $k = 1, \ldots, m$, $l = 1, \ldots, N^K_{dof}$, $n = 1, \ldots, d$.

The DG discretization of the viscous fluxes is based on the BR2 scheme, proposed in [20] and theoretically analyzed in [38] and [39]. According to this scheme, the viscous numerical flux is given by

$$\widehat{\mathbf{F}}_v\left(\mathbf{w}_h^{\pm}, (\nabla_h \mathbf{w}_h + \eta_F \mathbf{r}_F([\![\mathbf{w}_h]\!]))^{\pm}\right) \stackrel{\text{def}}{=} \{\mathbf{F}_v(\mathbf{w}_h, \nabla_h \mathbf{w}_h + \eta_F \mathbf{r}_F([\![\mathbf{w}_h]\!]))\} \tag{23}$$

where the stability parameter η_F is defined according to [39].

The inviscid numerical flux is computed from the solution of local Riemann problems in the normal direction at each integration point on elements faces. For compressible flows, we use either the exact Riemann solver of Gottlieb and Groth, [40], or, alternatively, the van Leer flux vector splitting method as modified by Hänel et al., [41]. For incompressible flows, we employ the approach proposed by Bassi et al. in [18], whereby the inviscid numerical flux $\widehat{\mathbf{F}}_c(\mathbf{w}_h^{\pm}) = \mathbf{F}_c(\mathbf{w}_h^*)$ is computed from the exact solution $\mathbf{w}_h^*$ of local Riemann problems suitably modified by means of an artificial compressibility perturbation, c^2. The details of the procedure for the determination of the state $\mathbf{w}_h^* = \mathbf{w}\left(\mathbf{w}_h^{\pm}, c^2\right)$ are thoroughly discussed in Appendix A of [18] for the case of the incompressible Euler equations as well as for the Stokes and Oseen equations. We remark that in this approach the artificial compressibility is only introduced locally to allow the evaluation of the convective numerical flux and no pressure time derivative is added to the DG discretized continuity equation, thus preserving the time accuracy of the method. According to the results of numerical experiments presented in [18] and [7], the value of the artificial compressibility parameter c^2 can be chosen in the range $[0.01, 100]$, without affecting the numerical accuracy. For the incompressible flow computations presented in this work the value was set equal to 0.1. The DG discretization is best suited for a weak enforcement of boundary conditions, [20, 19, 23]. This can easily be attained by properly defining boundary states and their gradients, which are used, directly or together with the internal states and their gradients, to compute the numerical inviscid and viscous fluxes and the lifting operators for all $F \in \mathcal{F}_h^b$. The boundary states and their derivatives must be defined according to the boundary types and, together with the internal states, enter in the Riemann solvers and ensure that the computed numerical fluxes are consistent with the physical ones.

3.3. Accurate time integration

Numerical integration of Eq. (22) by means of suitable Gauss quadrature rules leads to a system of nonlinear ODEs, or DAEs for incompressible flows, that can be written as

$$\mathbf{M_P}\left(\mathbf{W}\right)\frac{d\mathbf{W}}{dt} + \mathbf{R}\left(\mathbf{W}\right) = \mathbf{0}, \tag{24}$$

where $\mathbf{R}\left(\mathbf{W}\right)$ is the vector of residuals and $\mathbf{M_P}\left(\mathbf{W}\right)$ is a global block diagonal matrix arising from the discretization of the first integral in Eq. (22). When using the set of the compressible $\mathbf{w}_c$ and incompressible $\mathbf{w}_p$ flow variables together with the set of orthonormal basis functions outlined in Sec. 3.1, the matrix $\mathbf{M_P}$ reduces to the identity matrix and to a modified identity matrix, with zeros in the diagonal positions corresponding to the pressure degrees of freedom, respectively. However, for different sets of variables, the transformation matrix $\mathbf{P}$ couples the degrees of freedom of the variables $\mathbf{w}_h$ within each block of $\mathbf{M_P}$, so that this matrix can not be diagonal, even using a set of orthogonal basis functions. According to [23], implicit and accurate time integration of Eq. (24) can be efficiently performed by means of linearly implicit Rosenbrock-type Runge–Kutta schemes. We opted for this class of temporal schemes for four attractive features: (i) they have excellent stability properties; (ii) they are self-starting; (iii) they can use variable time steps; (iv) the Jacobian matrix needs to be assembled and factored only once per time step. Properly dealing with the solution dependent block diagonal matrix $\mathbf{M_P}(\mathbf{W})$, see [23], and according to the implementation-oriented formulation reported by Hairer and Wanner [42], the time integration of the DG space discretized equations with an s-stage Rosenbrock scheme can be written as

$$\mathbf{W}^{n+1} = \mathbf{W}^n + \sum_{j=1}^{s} m_j \mathbf{Y}_j, \tag{25}$$

$$\left(\frac{\mathbf{I}}{\gamma\Delta t} + \widetilde{\mathbf{J}}\right)^n \mathbf{Y}_i = -\widetilde{\mathbf{R}}\left(\mathbf{W}^n + \sum_{j=1}^{i-1} a_{ij}\mathbf{Y}_j\right) + \sum_{j=1}^{i-1}\frac{c_{ij}}{\Delta t}\mathbf{Y}_j, \quad i = 1,\ldots,s, \tag{26}$$

where, omitting the dependence on $\mathbf{W}$ for notational convenience,

$$\mathbf{J} = \frac{\partial\mathbf{R}}{\partial\mathbf{W}}, \qquad \widetilde{\mathbf{R}} = \mathbf{M_P}^{-1}\mathbf{R}, \qquad \widetilde{\mathbf{J}} = \frac{\partial\widetilde{\mathbf{R}}}{\partial\mathbf{W}} = \mathbf{M_P}^{-1}\left(\mathbf{J} - \frac{\partial\mathbf{M_P}}{\partial\mathbf{W}}\widetilde{\mathbf{R}}\right), \tag{27}$$

and m_i, a_{ij}, c_{ij} are real coefficients.

Recasting Eq. (26) so as to avoid the cumbersome product $\mathbf{M_P}^{-1}\mathbf{J}$ in Eq. (27), we obtain the final form used for the implementation [23]

$$\mathbf{W}^{n+1} = \mathbf{W}^n + \sum_{j=1}^{s} m_j \mathbf{Y}_j, \tag{28}$$

$$\left(\frac{\mathbf{M_P}}{\gamma\Delta t} + \mathbf{J} - \frac{\partial \mathbf{M_P}}{\partial \mathbf{W}}\widetilde{\mathbf{R}}\right)^n \mathbf{Y}_i = -\mathbf{M_P}^n\left[\widetilde{\mathbf{R}}\left(\mathbf{W}^n + \sum_{j=1}^{i-1} a_{ij}\mathbf{Y}_j\right) - \sum_{j=1}^{i-1}\frac{c_{ij}}{\Delta t}\mathbf{Y}_j\right], \quad i = 1, \ldots, s, \tag{29}$$

which also allows to quantify the computational overhead due to the solution dependent block diagonal matrix $\mathbf{M_P}$. We remark that our implementation relies on an analytical derivation of the Jacobian matrix $\mathbf{J}$ that takes fully account of the dependence of the vector of the residuals on the unknowns and their derivatives, including the implicit treatment of lifting operators and boundary conditions. The linear problems in Eq. (29) can be efficiently solved in parallel by means of the matrix-explicit or the matrix-free GMRES method included in the PETSc library [43, 44]. Preconditioning by using the block Jacobi method with one block per process, each solved with ILU(0), or the Additive Schwarz Method (ASM) is usually employed to make GMRES convergence acceptable for complex problems.

In the following, to keep the notation as simple as possible, we will refer to the Rosenbrock schemes as ROq-s, where q is the order of convergence and s is the number of stages. In this work we employ the schemes RO2-2 of Iannelli and Baker, [45], RO3-3 (ROS3P) of Lang and Verwer, [46], and RO5-8 (RODAS5(4)-Rod5_1) of Di Marzo, [47]. All these schemes are designed to preserve their accuracy with DAEs.

The authors in [23] investigated the temporal accuracy and performance of several Rosenbrock schemes (up to order six) for the computation of both compressible and incompressible flows. Their numerical investigation demonstrated that higher-order schemes are much more efficient than lower-order ones if low levels of time integration error, as those required by DNS and LES, are being sought. In the same paper the coefficients of all the considered schemes are also tabulated. An example of an indirect proof of order assessment, based on the error introduced by the time integration scheme in fulfilling the discretized incompressibility constraint, is given for a complex three dimensional problem in [48].

A simple approach to dense output, based on a fifth-degree polynomial interpolation of the solution within the time step, and where coefficients are obtained by imposing the solution and its first and second time derivatives at the time step extrema, is reported in Appendix A.1. This interpolation technique is suitable for any implicit time integration scheme that relies on an exact Jacobian matrix evaluation.

4. Numerical results

In this section we demonstrate the reliability of the proposed coupling between a high-order Rosenbrock scheme and a high-order DG space discretization applied to DNS and ILES. To this purpose, two well-established flow problems, one compressible and one incompressible, have been computed and results presented below.

The former concerns the DNS of the incompressible flow past a sphere at a diameter-based Reynolds number of $\mathrm{Re}_D = 1000$. For this test case the simulations have been performed with two different temporal schemes and polynomial degree of the DG space approximation. The latter is the ILES of the transitional flow around the SD7003 airfoil at a chord-based Reynolds number of $\mathrm{Re}_c = 60000$. In this case we computed the solution on two meshes with different polynomial degrees and a very highly accurate time integration scheme, *i.e.* the RO5-8, to assess the influence of p- and h- refinement.

Both the test cases have been run in parallel, using up to 4096 CPU cores, on the CINECA IBM-BlueGene/Q supercomputer named FERMI.

4.1. Flow past a sphere at $\mathrm{Re}_D = 1000$

In this section the assessment of our DG solver for the DNS of an incompressible transitional flow is reported. Few papers have been published on DG methods applied to DNS, see, *e.g.* [10, 49, 50, 12], and, up to authors knowledge, they are restricted to compressible flows.

The incompressible flow past a sphere has been computed at a diameter-based $\mathrm{Re}_D = 1000$ on the computational mesh made of 57600 20-node hexahedral elements (quadratic edge representation) and first cell height $\Delta n/D = 0.005$ shown in Figure 1. The computations have been performed with a free-stream velocity aligned with the x_3 axis on exactly the same cylindrical domain used by Toumboulides and Orszag [51]. The cylinder radius is $4.5D$, the inflow boundary is located $4.5D$ upstream from the sphere, and the outflow boundary is placed $25D$ downstream from the sphere, thus a long wake can be accurately computed. In fact, at this flow conditions the laminar to turbulent transition takes place in the sphere wake.

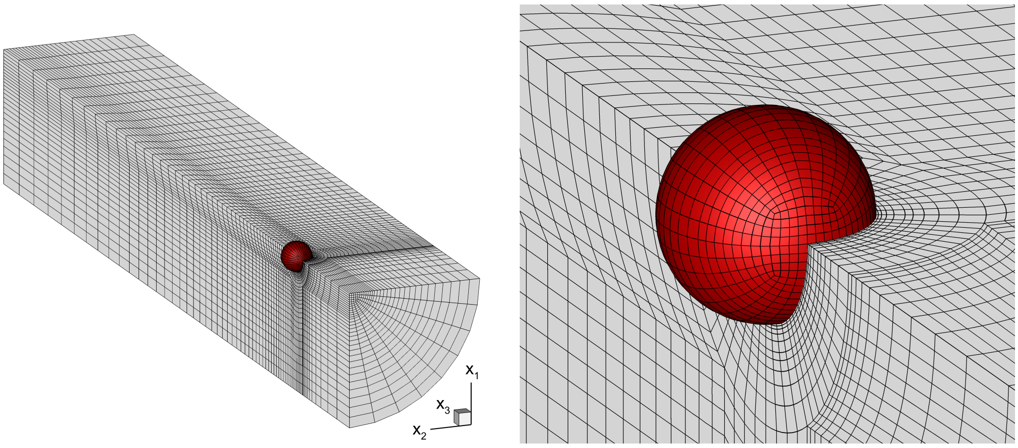

(a) detail of the computational domain

(b) detail of the sphere surface mesh

Figure 1: Flow past a sphere - Computational mesh with 57600 20-node hexahedral elements (quadratic edges)

The test case has been computed by using the RO2-2 scheme of Iannelli and Baker, [45], and the RO3-3 scheme of of Lang and Verwer, [46], coupled with $\mathbb{P}^3$ and $\mathbb{P}^4$ DG space approximations, respectively. The solutions have been advanced in time with a fraction $f = 4\text{e}{-3}$ of the convective time, *i.e.*, $\Delta t = f(D/u_\infty)$ and initialized by a $\mathbb{P}^3$ $\mathrm{Re}_D = 250$ steady solution. Turbulence statistics have been computed for $130D/u_\infty$ time units after the appearance of distorted hairpin vortices in the wake region.

Both the RO2-2-DG $\mathbb{P}^3$ and the RO3-3-DG $\mathbb{P}^4$ time averaged and root mean square distributions of velocity downstream of the sphere along the x_3 axis are in good agreement with the experimental results of Wu and Faeth [52] obtained for $\mathrm{Re}_D = 960$, see Figure 2. The results are also in satisfactory agreement with the numerical computations of Tomboulides and Orzsag [51]. Figure 3 shows the time averaged and root mean square radial distributions of u_3 at different x_3 locations. Although noticeable differences are observed between the $\mathbb{P}^3$ and $\mathbb{P}^4$ solutions the

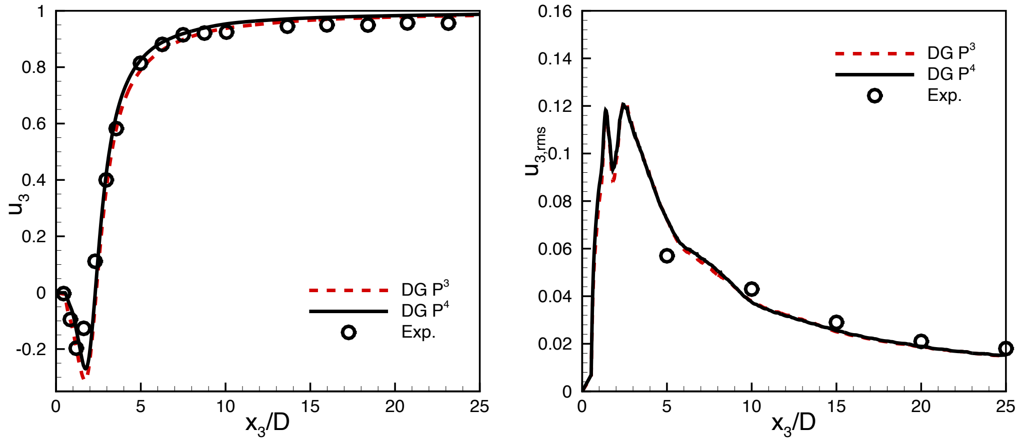

(a) time average (b) root mean square

Figure 2: Flow past a sphere - Time averaged and root mean square distributions of u_3 along the x_3 axis downstream of the sphere (experimental data of Wu and Faeth [52] obtained by digitalizing the paper of Tomboulides and Orzsag [51])

higher-order results are similar to the computations of Tomboulides and Orzsag [51]. We remark

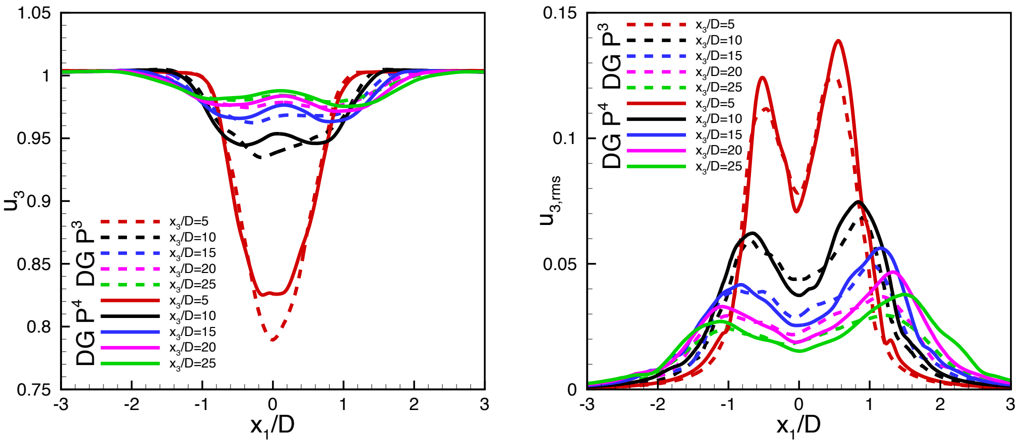

(a) time average (b) root mean square

Figure 3: Flow past a sphere - Time averaged and root mean square distributions of u_3 along the radial direction at different x_3 locations

that, due to the limited simulation time dedicated to compute the turbulence statistics, our results are not perfectly symmetrical with respect to the x_3 axis. The continuation of our computations is the subject of ongoing work.

At these flow conditions the wake is essentially axisymmetric in an averaged sense, as confirmed by the energy power spectra at four points located at the same x_3 and radial $r = (x_1^2+x_2^2)^{1/2}$ position but with different azimuthal coordinates, $\theta = \tan^{-1}(x_2/x_1)$, see Figure 4(a). The energy power spectrum is here computed as $(\mathrm{PSD}(u_1) + \mathrm{PSD}(u_2) + \mathrm{PSD}(u_3))/2$, where u_i is the temporal signal of the i-component of the velocity. For a point located downstream from the sphere and not laying on the wake axis, Figure 4(b) displays the influence of the solution accuracy on the spectrum. We remark that, although the decay spectrum has the expected slope of $-5/3$ for both the solutions, while for low frequencies the results are almost indistinguishable, for higher frequencies the RO3-3–DG $\mathbb{P}^4$ spectrum is slightly shifted to the right side. This difference is noticeably smaller than what we observed for the ILES application reported in the following section, see Figure 14. A similar behaviour is also observed for the energy spectra shown in a recent paper of Chapelier et al. [12] on DG applied to DNS, where the authors computed the Taylor-Green vortex and channel flow using a compressible explicit in time solver. Our spectra confirm that close to the sphere the results have to be considered as a DNS, however, far from the sphere, where for computational efficiency reasons the grid size has been sightly increased, it is possible that not all the turbulent scales have been fully resolved, thus explaining the differences between the RO2-2–DG $\mathbb{P}^3$ and RO3-3–DG $\mathbb{P}^4$ solutions shown in Figure 3 and Figure 4(b).

Figure 4(c) shows the power spectra at four points on the x_3 axis at different distances downstream from the sphere. At $x_3/D = 1.5$, within the recirculation zone in the separated region, the spectrum does not follow the $-5/3$ law, thus confirming that separation occurs in the laminar regime and than develops in a turbulent wake, see also Figure 4(d). The time averaged drag coefficient, and the Strouhal number corresponding to the shedding frequency of the hairpin vortex shown in Figure 5, are tabulated in Table 1. The computed values are in good agreement with published data and show the beneficial effect of increasing the solution accuracy.

4.2. *Transitional flow around the SD7003 airfoil*

The ILES of the transitional compressible flow around the SD7003 airfoil, one of the test cases proposed within the “International Workshop on High-Order CFD Methods” [57], is here considered. As ILES does not include any explicit SGS model and the discretization itself acts like a subgrid-scale model, the flow equations are simply the DG space discretized compressible

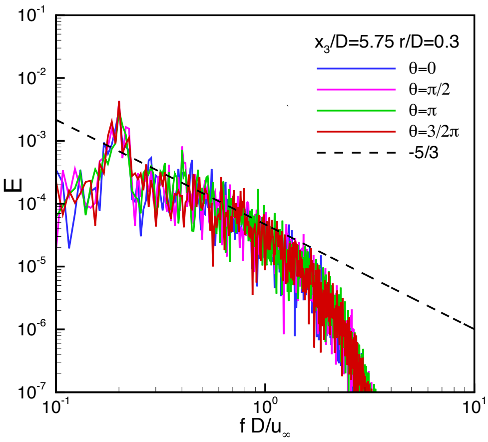

(a) axisymmetric flow, $\mathbb{P}^4$ solution

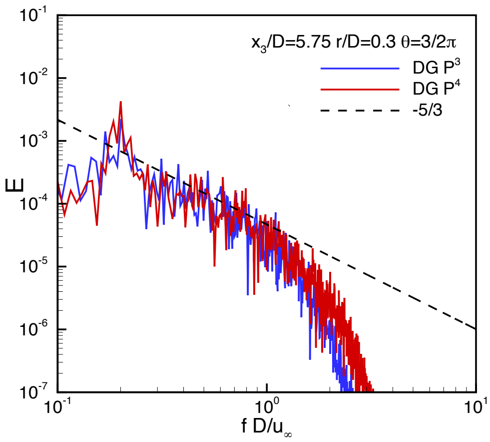

(b) influence of the order of accuracy

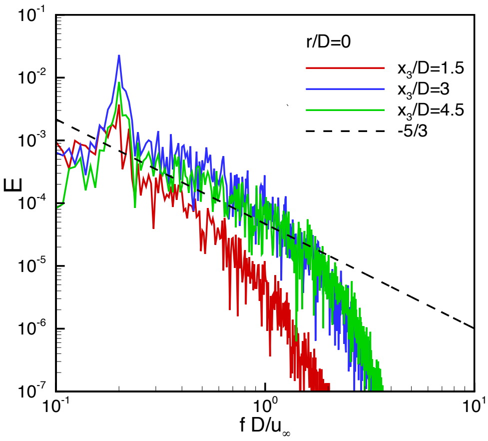

(c) wake development on x_3 axis, $\mathbb{P}^4$ solution

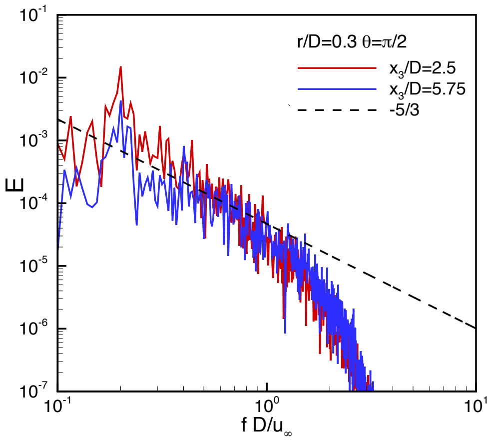

(d) wake development at $r/D = 0.3$ and $\theta = \pi/2$, $\mathbb{P}^4$ solution

Figure 4: Flow past a sphere - Energy power spectra for different locations in the wake and different polynomial degrees

Navier–Stokes equations integrated in time by means of a very high-order temporal scheme. The main difficulties of this challenging test case are related to the complex physical features of an unsteady flow characterized by a laminar separation, *i.e.* the formation of a transitional shear layer followed by turbulent reattachment on the suction side of the wing by virtue of the enhanced momentum transport.

To investigate the influence of p- and h- refinement on ILES, the flow around the SD7003 airfoil has been computed for the conditions $\mathrm{M}_\infty = 0.1$, $\alpha = 8^\circ$ and chord-based $\mathrm{Re}_c = 60000$

	C_D	St
RO2-2-DG $\mathbb{P}^3$	0.471	0.201
RO3-3-DG $\mathbb{P}^4$	0.475	0.200
Hindenlang et al. [53]	0.48	–
Ploumhans et al. [54]	0.48	–
Tomboulides and Orzsag [51]	–	0.195
Poon et al. [55]	0.46	0.20
Sakamoto and Haniu [56] (Exp.)	–	0.195–0.205

Table 1: Flow past a sphere - Time averaged drag coefficient and Strouhal number

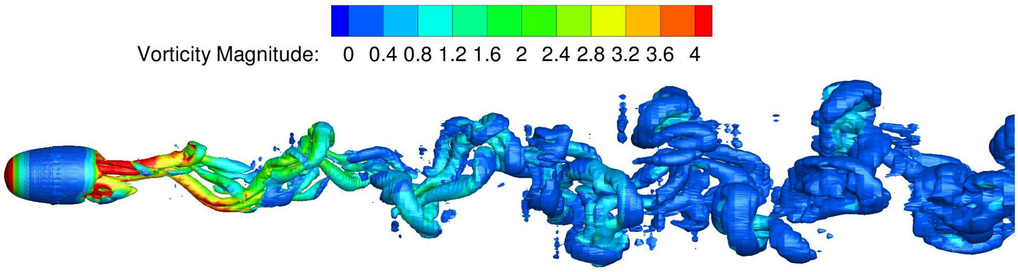

Figure 5: Flow past a sphere - Instantaneous $\lambda_2 = 1\text{e}{-3}$ isosurface of λ_2-criterion coloured with the non-dimensional vorticity magnitude

with different DG space approximations on a coarse mesh of 20064 50-node hexahedral elements (quartic edge representation) and on a uniformly refined mesh of 160512 20-node hexahedral elements (quadratic edge representation) with a first cell height of $\Delta n/c = 2.9\text{e}{-4}$ and of $\Delta n/c = 1.45\text{e}{-4}$, respectively. The computational grids are shown in Figure 6. This low Mach number value has been chosen to compare our solutions with the computational results presented in the literature, *e.g.* [58, 59]. A no-slip isothermal wall condition with $T_{wall}/T_\infty = 1.002$ is imposed at the airfoil surface, while a periodic boundary condition over a width $s/c = 0.2$ is set in the spanwise direction to emulate an infinite wing. At the farfield boundary, located $\sim 100\,c$ from the wing, characteristic-based conditions have been imposed. The test case has been computed with the RO5-8 time-integration scheme of Di Marzo, see [47], coupled with $\mathbb{P}^3$ and $\mathbb{P}^4$ DG space approximations on the coarse mesh, and with $\mathbb{P}^2$ and $\mathbb{P}^3$ approximations on the fine mesh. The number of degrees of freedom per equation (DOFs) of these solutions is reported in Table 2 together with the results available in the literature. On the coarse mesh the solutions have been

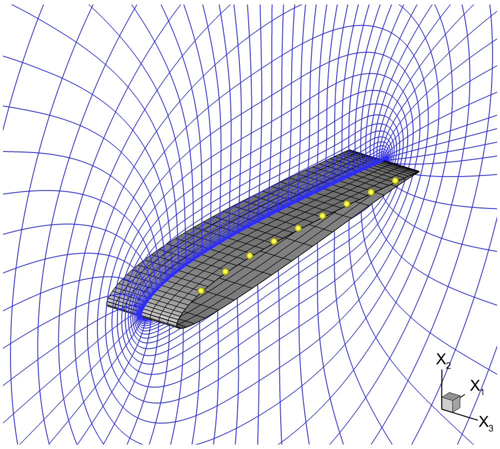

(a) 20064 hexahedral el. quartic edges

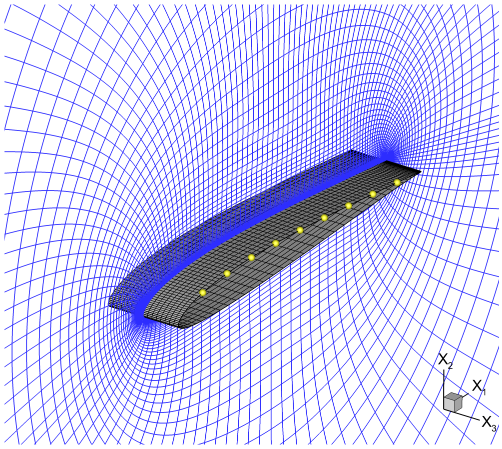

(b) 160512 heahedral el. quadratic edges

Figure 6: SD7003 - Computational meshes, the yellow spheres indicate the chordwise locations of the measured velocity profiles

advanced in time with a time step equal to a fraction $f = 4.4\mathrm{e}{-3}$ of the convective time, *i.e.*, $\Delta t = f\,(c/u_\infty)$, while on the fine mesh the values $f = 4.4\mathrm{e}{-3}$ and $f = 2.2\mathrm{e}{-3}$ have been used for the $\mathbb{P}^2$ and $\mathbb{P}^3$ space approximation, respectively. All the computations have been initialized from a p-sequence of lower-order, not fully statistically converged solutions. Figures 7 and 8 show the contours of the mean pressure coefficient and of the mean x_1-component of velocity around the airfoil. A detailed view of the flow field and of detachment and reattachment points of the laminar separation bubble (LSB) is shown in Figure 9. The term "mean" denotes solutions averaged both in time and in the spanwise direction. A rigorous yet practical approach to the spatial averaging in a modal DG framework is reported in Appendix A.2.

To assess the influence of p- and h- refinement on our computations we assume as reference the $\mathbb{P}^3$ solution obtained on the fine mesh with the halved time step. The dimensions of the laminar separation bubble reported in Table 2, along with the mean skin friction and pressure coefficient distributions shown in Figure 11, highlight the noticeable difference between the LSB size predicted on the coarse grid by the $\mathbb{P}^3$ approximation and the other more accurate solutions. We remark that our $\mathrm{C_p}$ and $\mathrm{C_f}$ distributions are in fair agreement with the incompressible LES of Catalano and Tognaccini obtained using second-order central differences in streamwise and wall-normal directions, and Fourier collocations in the spanwise direction, on a grid with 864

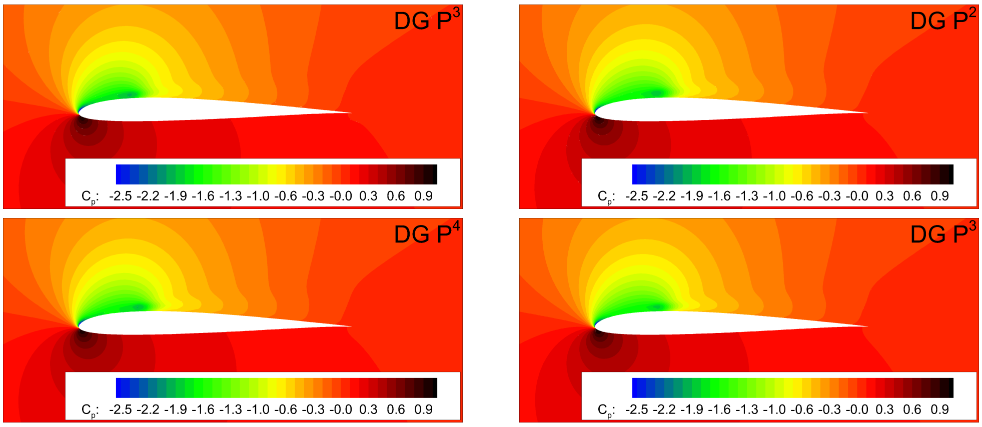

(a) coarse mesh, RO5-8–DG $\mathbb{P}^{3,4}$ solutions (b) fine mesh, RO5-8–DG $\mathbb{P}^{2,3}$ solutions

Figure 7: SD7003 - Contours of mean pressure coefficient

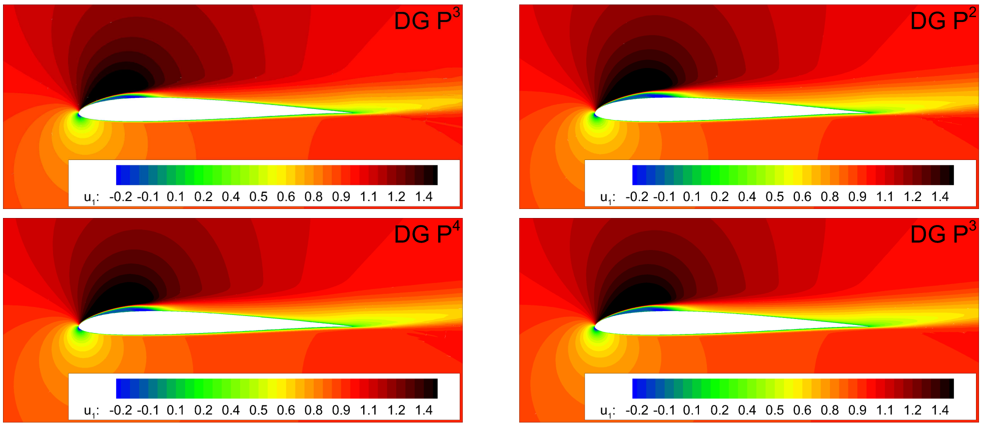

(a) coarse mesh, RO5-8–DG $\mathbb{P}^{3,4}$ solutions (b) fine mesh, RO5-8–DG $\mathbb{P}^{2,3}$ solutions

Figure 8: SD7003 - Contours of mean x_1-component of velocity

cells in the streamwise, 208 in the crosswise, and 48 in the spanwise direction [60]. The lack of spatial resolution of our $\mathbb{P}^3$ approximation is confirmed by the significant difference between the predicted mean velocity profiles and the reference, see Figure 10. The profiles have been extracted along vertical lines at the chordwise locations indicated in Figure 6. We remark that, although having less DOFs per equation than the $\mathbb{P}^2$ solution on the fine mesh, roughly the 56% less, the $\mathbb{P}^4$ results on the coarse grid are closer to the reference, both in terms of LSB dimensions and mean velocity profiles, thus suggesting that increasing the degree of the

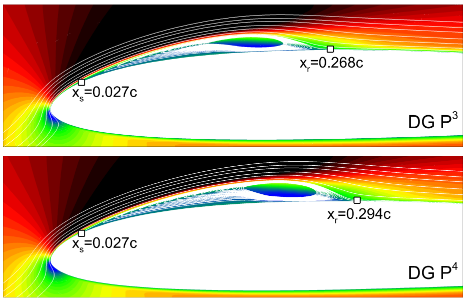

(a) coarse mesh, RO5-8–DG $\mathbb{P}^{3,4}$ solutions

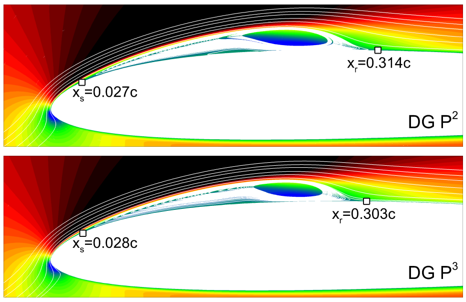

(b) fine mesh, RO5-8–DG $\mathbb{P}^{2,3}$ solutions

Figure 9: SD7003 - Contours of mean x_1-component of velocity, detail of the laminar separation bubble with indication of the separation and reattachment points

	DOFs	LSB details				Aerodynamic loads		
		x_s/c	x_r/c	L/c	H/c	C_D	C_L	C_m
RO5-8–DG $\mathbb{P}^3$ coarse	401280	0.027	0.268	0.241	0.017	0.0423	0.9615	-0.0233
RO5-8–DG $\mathbb{P}^4$ coarse	702240	0.027	0.294	0.267	0.021	0.0454	0.9534	-0.0224
RO5-8–DG $\mathbb{P}^2$ fine	1605120	0.027	0.314	0.287	0.022	0.0471	0.9548	-0.0235
RO5-8–DG $\mathbb{P}^3$ fine	3210240	0.028	0.303	0.275	0.021	0.0457	0.9441	-0.0223
DGSEM $\mathbb{P}^3$ [59]	4.26M	0.027	0.310	-	-	0.045	0.923	-
DGSEM $\mathbb{P}^7$ [59]	4.55M	0.030	0.336	-	-	0.050	0.932	-
Comp. FD $\mathcal{O}(6)$ [58]	53.4M	0.031	0.303	0.272	0.020	0.0447	0.917	-0.0187
SBP-SAT $\mathcal{O}(4)$ [61]	4.48M	0.037	0.200	-	-	0.034	0.968	-

Table 2: SD7003 - Details of the laminar separation bubble and mean aerodynamic loads. x_s and x_r are the separation and reattachment points coordinates, L and H the separation bubble length and height

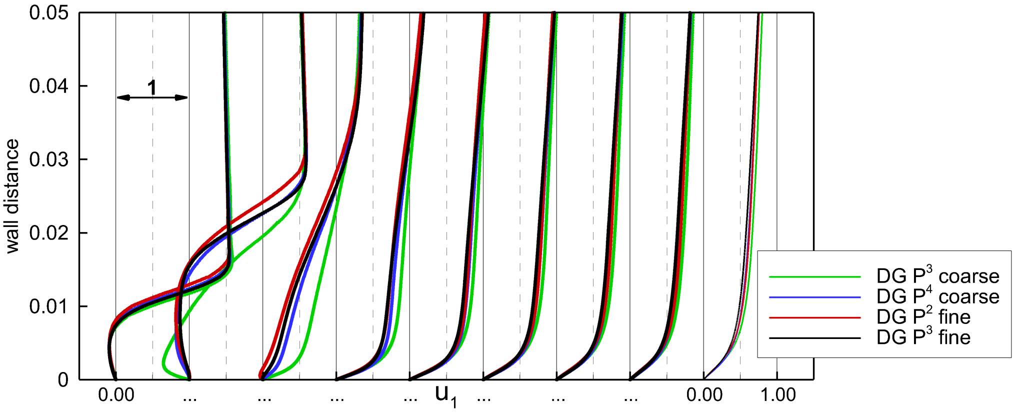

Figure 10: SD7003 - Profiles of mean x_1-component of velocity at chordwise locations $x_1/c = \{0.1, \ldots, 0.9\}$, coarse mesh RO5-8–DG $\mathbb{P}^{3,4}$ and fine mesh RO5-8–DG $\mathbb{P}^{2,3}$ solutions

polynomial DG space approximation is better than refining the mesh. The mean drag, lift and moment coefficients of the airfoil are reported in Table 2.

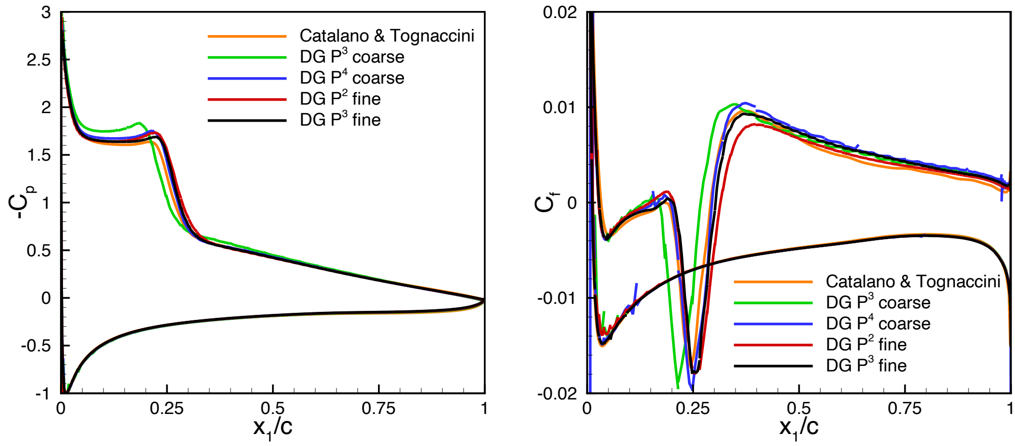

Figure 11: SD7003 - Mean C_p and C_f distributions, coarse mesh RO5-8–DG $\mathbb{P}^{3,4}$ and fine mesh RO5-8–DG $\mathbb{P}^{2,3}$ solutions

The same beneficial effect of a higher-degree polynomial approximation on the solution is observed for the instantaneous $Q = 500$ isosurface of Q-criterion displayed in Figure 13, and for the contours of spanwise-averaged Reynolds stress component $< u'_1 u'_1 >$ in Figure 12. In fact, the $\mathbb{P}^4$ solution on the coarse mesh, compared to the $\mathbb{P}^3$ on the same mesh and also to the $\mathbb{P}^2$ on the finer grid, is able to solve much better the small vortical structures above the airfoil and to provide a distribution of the mean squared fluctuation of x_1-velocity closer to the reference result and noticeably less diffused than the $\mathbb{P}^2$ computation. Figure 14 displays the influence of p- or h- refinement on the energy spectrum for different chordwise locations. The spectra have been computed as $1/n_k \sum_{k=1}^{n_k}((\mathrm{PSD}(u_{1,k}) + \mathrm{PSD}(u_{2,k}) + \mathrm{PSD}(u_{3,k}))/2)$, where n_k is the number of equally spaced points used for averaging in the spanwise direction, and $u_{i,k}$ is the temporal signal of the i-component of the velocity at the k^{th} spanwise position. The n_k value was set equal to 104 and 2048 for the computations on the coarse and on fine grid, respectively. We remark that for both the meshes the onset of dissipation is pushed towards higher frequencies by the higher-order solutions. Although having far less DOFs the cut-off level of the coarse $\mathbb{P}^4$ solution is comparable and even better than the $\mathbb{P}^2$ solution on the fine mesh, thus confirming that, at least for this test case, p-refinement is preferable to h-refinement in terms of global solution accuracy.

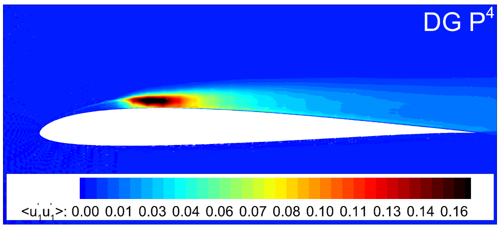

(a) coarse mesh, RO5-8–DG $\mathbb{P}^4$ solution

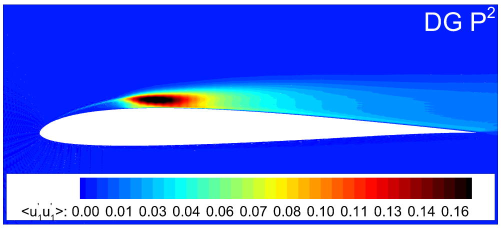

(b) fine mesh, RO5-8–DG $\mathbb{P}^2$ solution

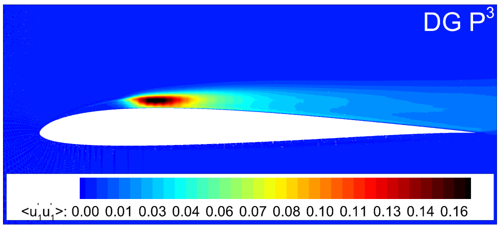

(c) fine mesh, RO5-8–DG $\mathbb{P}^3$ solution

Figure 12: SD7003 - Contours of spanwise-averaged Reynolds stress $< u_1' u_1' >$

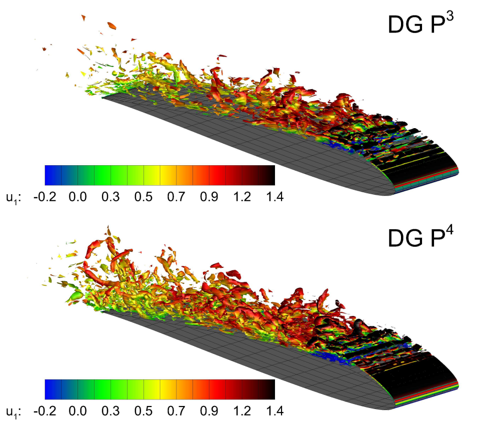

(a) coarse mesh, RO5-8–DG $\mathbb{P}^{3,4}$ solutions

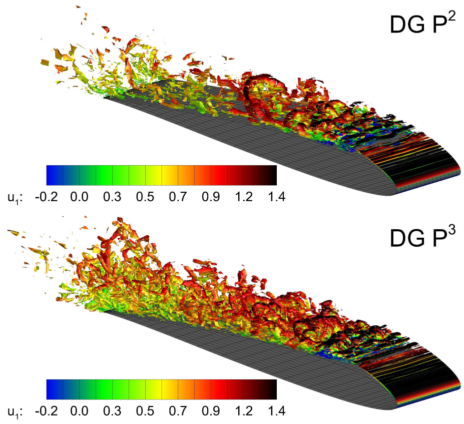

(b) fine mesh, RO5-8–DG $\mathbb{P}^{2,3}$ solutions

Figure 13: SD7003 - Instantaneous $Q = 500$ isosurface of Q-criterion

Due to the great computational resources required for a thorough analysis, the evaluation of the computational cost related to the higher-order DG space solutions in the DNS and LES context has been left for future work.

The presence of a challenging flow feature such as the laminar separation bubble makes this test case very well suited for assessing the accuracy of different LES approaches but, unfortu-

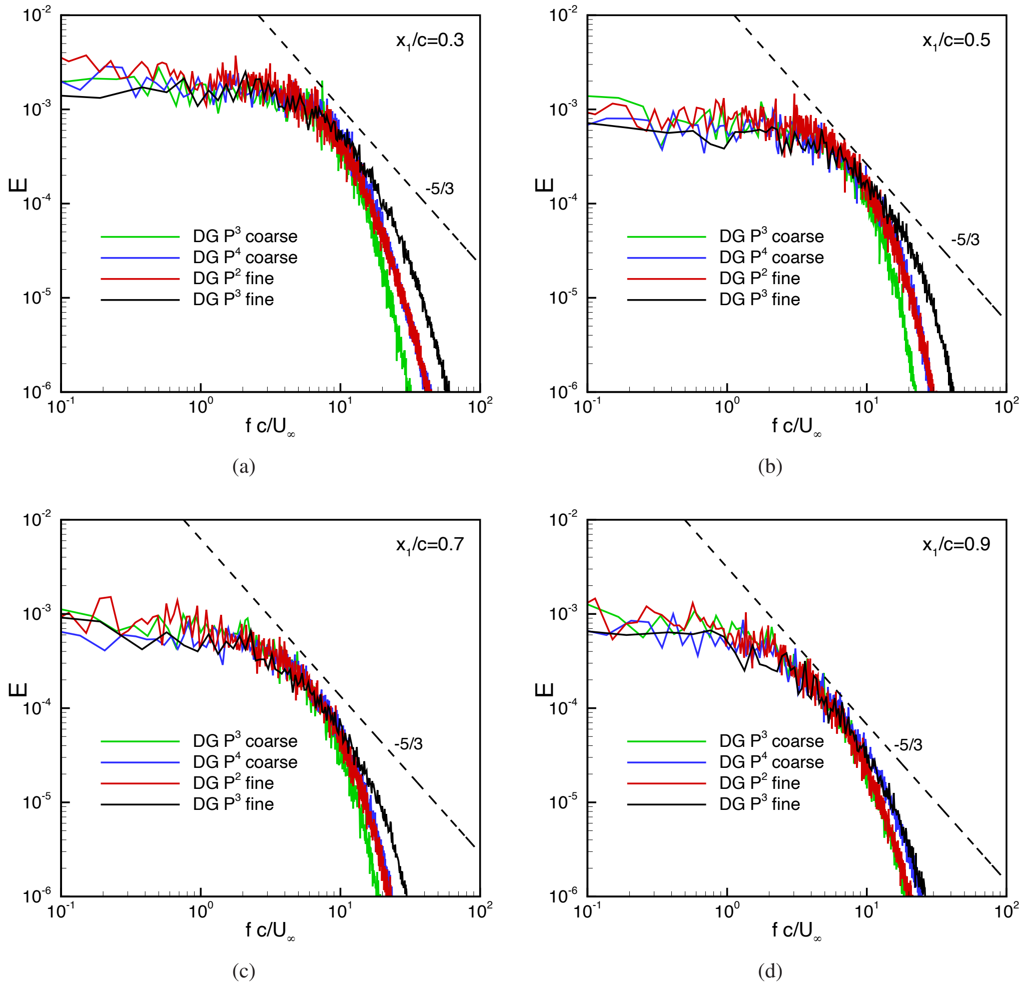

(a) (b) (c) (d)

Figure 14: SD7003 - Energy power spectra at chordwise locations $x_1/c = \{0.3, 0.5, 0.7, 0.9\}$

nately, no reference DNS database is available and the several published LES results show a certain dispersion. Nevertheless the results here presented are reasonably in good agreement with those reported by other authors in [60, 58, 59] and confirm the suitability of high-order DG methods for this very promising approach to the solution of turbulent flows.

5. Conclusions

In this paper the potential of our DG solver in the context of the DNS and ILES has been investigated. Thanks to its great flexibility, the proposed implementation allows to handle, within a unified numerical framework, both compressible and incompressible flows. The employed DG method also allows to compute very high-order accurate solutions, both in space and time, on curved, possibly hybrid, computational grids, without being affected by the quality of the mesh elements and the domain complexity.

Our numerical computations have been compared with experimental and numerical results available in the literature, showing a good agreement and confirming the great accuracy and the good dissipation and dispersion properties of DG method. This paper also proves the reliability and robustness of our implementation in dealing with large problems on massively parallel architectures, here up to 4096 cores.

Ongoing work is devoted to further investigate DNS and ILES on canonical test cases, *e.g.* channelflow, to assess whether the DNS- and ILES-DG methods can really compete with state-of-the-art high-accuracy solvers and SGS models. The assessment of code scalability on very large problems, ten of thousands cores, and the study of hybrid MPI/OpenMP programming paradigms is left for future work.

Acknowledgements

This work was carried out within the EU FP7 IDIHOM project [62]. We acknowledge the CINECA awards under the LISA (HPL13PCW5H) and ISCRA (HP10CIP427) initiatives, and the resources provided by CINECA within the "Convenzione di Ateneo Università degli Studi di Bergamo", for the availability of high performance computing and support. We also acknowledge Dr. P. Catalano and Dr. R. Tognaccini for providing us their SD7003 numerical results for comparison purpose.

Appendix A. Notes on flow statistics computation

Appendix A.1. Dense output for implicit time integration schemes

Thanks to their favourable stability properties implicit time integration schemes allow using large time steps. However, during time-accurate simulations, one can be interested in the numerical solution at some time instant $t^* = (1-\theta)t^n + \theta t^{n+1}$, $0 < \theta < 1$, between t^n and t^{n+1}.

The dense output serves to provide, with a low additional computational cost, an accurate numerical approximation of the solution for any $0 \le \theta \le 1$, see [63, 42, 64] for an extensive review on this topic. In the following the same notation of Sec. 3.3 is used.

In this work we obtain an up to fifth-degree polynomial representation of any component w_h of the solution vector $\mathbf{w}_h$ (for the sake of compactness we drop the variable index j) within the time step Δt, by considering a polynomial interpolation of the solution in time

$$w_h(\theta) = \psi_l(\theta)\, a_l, \quad \forall \theta \in [0, 1], \tag{A.1}$$

where, repeated indices imply summation over the range $l = 1, \ldots, N_{dof}$ and basis functions ψ_l can be chosen independently from those used for the space discretization, *e.g.* monomials. The interpolation can be applied componentwise to $\mathbf{W}$, thus obtaining the global vector of degrees of freedom at any intermediate time level θ. The coefficients of the expansion a_l are explicitly calculated by imposing the solution value and its first and second derivatives in time at the time step extrema. In fact, time derivatives are available, or easily computable, during the time integration according to

$$\frac{d\mathbf{W}}{dt} = -\widetilde{\mathbf{R}}, \tag{A.2}$$

$$\frac{d^2\mathbf{W}}{dt^2} = -\frac{\partial \widetilde{\mathbf{R}}}{\partial t} = -\frac{\partial \widetilde{\mathbf{R}}}{\partial \mathbf{W}}\frac{d\mathbf{W}}{dt} = \widetilde{\mathbf{J}\mathbf{R}}. \tag{A.3}$$

While the computation of the residual $\widetilde{\mathbf{R}}$ can be considered as part of the cost of the time integration scheme, this approach to dense output requires the additional evaluation of the matrix-vector product $\widetilde{\mathbf{J}\mathbf{R}}$ at each time step. Finally, we remark that this simple interpolation technique can be applied to any implicit time integration scheme that relies on an exact Jacobian matrix evaluation.

Appendix A.2. Spatial average in the modal DG framework

In this paper we propose a rigorous yet practical approach to the spatial average that can easily be applied to a DG method that uses modal basis functions. The idea is to solve an auxiliary linear problem for computing the integral I of an arbitrary function w along a given direction $\boldsymbol{a} \in \mathbb{R}^d$. In the following the same notation of Sec. 3.2 is used.

Here the function $w \in \mathbb{R}$ is any component of the solution vector $\mathbf{w}$ (for the sake of notation clarity we drop the variable index j), for which we solve the following equation

$$a_j \frac{\partial I}{\partial x_j} - w = 0, \tag{A.4}$$

where $I \in \mathbb{R}$, and repeated indices imply summation over the range $j = 1, \ldots, d$. By multiplying Eq. (A.4) by an arbitrary smooth test function v and integrating by parts, the weak formulation reads

$$\int_{\partial\Omega} vI \left(\boldsymbol{a} \cdot \mathbf{n}\right) d\sigma - \int_{\Omega} I \left(\boldsymbol{a} \cdot \nabla v\right) d\mathbf{x} - \int_{\Omega} vw d\mathbf{x} = 0. \tag{A.5}$$

We substitute the solution and the test function with the finite element approximations I_h and v_h, both belonging to the space $V_h \stackrel{\text{def}}{=} \mathbb{P}^k_d(\mathcal{T}_h)$. By using the same set of shape functions of Sec. 3.2 and splitting integrals over mesh elements and faces we obtain

$$\sum_{F \in \mathcal{F}_h} \int_F [\![\phi_i]\!]_j \, a_j \hat{I}\left(I_h^{\pm}\right) d\sigma - \sum_{K \in \mathcal{T}_h} \int_K \frac{\partial \phi_i}{\partial x_j} a_j I_h d\mathbf{x} - \sum_{K \in \mathcal{T}_h} \int_K \phi_i w_h d\mathbf{x} = 0, \tag{A.6}$$

for $i = 1, \ldots, N^K_{dof}$, where $\hat{I}\left(I_h^{\pm}\right)$ denotes a simple upwind evaluation of I_h at each integration point on faces. By expressing I_h in terms of the elements of a global vector $\mathbf{I}$ of unknown degrees of freedom, such that $I_h = \phi_l I_l$, $l = 1, \ldots, N^K_{dof}$, $\forall K \in \mathcal{T}_h$, the DG solution of A.4 consists in seeking the elements of $\mathbf{I}$ such that

$$\sum_{F \in \mathcal{F}_h} \int_F [\![\phi_i]\!]_j \, a_j \hat{I}\left((\phi_l \mathbf{I}_l)^{\pm}\right) d\sigma - \sum_{K \in \mathcal{T}_h} \int_K \frac{\partial \phi_i}{\partial x_j} a_j \phi_l \mathbf{I}_l d\mathbf{x} - \sum_{K \in \mathcal{T}_h} \int_K \phi_i \phi_l \mathbf{W}_l d\mathbf{x} = 0, \tag{A.7}$$

for $i = 1, \ldots, N^K_{dof}$, with homogeneous condition imposed at the inflow boundary, and where repeated indices imply summation over the range $l = 1, \ldots, N_{dof}^{K}$.

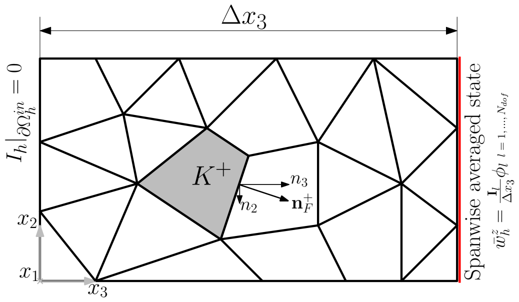

Figure A.15: Spatial average in the spanwise direction, x_3

In this paper we relied on the present approach for the computation of a spanwise averaged solution for the SD7003 testcase. According to the meshes reference frames the wing span is aligned with the x_3 direction, as represented in a simplify sketch in Figure A.15. The averaged solution $\bar{w}_h^z$ is then computed by solving the problem of Eq. A.7 with $\boldsymbol{a} = [0, 0, 1]$, by dividing the resulting array of the degrees of freedom $\mathbf{I}$ by the span, *i.e.* Δx_3, and finally obtaining the averaged state through the scaled $\mathbf{I}$ at the end of the wing

$$\bar{w}_h^z (x, y, \Delta x_3) = \frac{\mathbf{I}_l}{\Delta x_3} \phi_l (x, y, \Delta x_3), \quad \forall x, y \in \overline{\Omega}_h, \tag{A.8}$$

where, for the sake of clarity, the dependence of basis functions from the coordinates has been shown.

References

[1] F. Bassi, A. Crivellini, S. Rebay, M. Savini, Discontinuous Galerkin solution of the Reynolds-averaged Navier-Stokes and k-ω turbulence model equations, Comput. Fluids 34 (2005) 507–540.

[2] P. O. Persson, N. Nguyen, J. Peraire, RANS solutions using high order discontinuous Galerkin methods, AIAA Paper 2007-914 (2007).

[3] T. A. Oliver, D. L. Darmofal, An unsteady adaptation algorithm for discontinuous Galerkin discretizations of the RANS equations, AIAA Paper 2007-3940 (2007).

[4] N. K. Burgess, D. J. Mavriplis, Robust Computation of Turbulent flows using a Discontinuous Galerkin Method, 50th AIAA Aerospace Sciences Meeting including the New Horizons Forum and Aerospace Exposition AIAA 2012-0457 (2012).

[5] B. Landman, M. Kessler, S. Wagner, E. Krämer, A parallel, high-order discontinuous Galerkin code for laminar and turbulent flows, Comput. Fluids 37 (4) (2008) 427–438.

[6] R. Hartmann, J. Held, T. Leicht, Adjoint-based error estimation and adaptive mesh refinement for the RANS and k-ω turbulence model equations, J. Comput. Phys. 230 (2011) 4268–4284.

[7] A. Crivellini, V. D'Alessandro, F. Bassi, A Spalart-Allmaras turbulence model implementation in a discontinuous Galerkin solver for incompressible flows, J. Comput. Phys. 241 (2013) 388–415. doi:http://dx.doi.org/10.1016/j.jcp.2012.12.038.

[8] S. Schoenawa, R. Hartmann, Discontinuous Galerkin discretization of the Reynolds-averaged Navier-Stokes equations with the shear-stress transport model, J. Comput. Phys. 262 (0) (2014) 194 – 216. doi:http://dx.doi.org/10.1016/j.jcp.2013.12.062.

[9] F. Bassi, A. Ghidoni, A. Perbellini, S. Rebay, A. Crivellini, N. Franchina, M. Savini, A high-order Discontinuous Galerkin solver for the incompressible RANS and k-ω turbulence model equations, Comput. Fluids 98 (0) (2014) 54–68, 12th USNCCM mini-symposium on High-Order Methods for Computational Fluid Dynamics - A special issue dedicated to the 80th birthday of Professor Antony Jameson. doi:http://dx.doi.org/10.1016/j.compfluid.2014.02.028.

[10] S. S. Collis, Discontinuous Galerkin methods for turbulence simulation, in: Proceedings of the 2002 Center for Turbulence Research Summer Program 2002, 2002, pp. 115–167.

[11] S. S. Collis, The DG/VMS method for unified turbulence simulation, 32nd AIAA Fluid Dynamics Conference and Exhibit AIAA 2002-3124 (2002).

[12] J.-B. Chapelier, M. de la Llave Plata, F. Renac, E. Lamballais, Evaluation of a high-order discontinuous Galerkin method for the DNS of turbulent flows, Comput. Fluids 95 (0) (2014) 210 – 226. doi:http://dx.doi.org/10.1016/j.compfluid.2014.02.015.

[13] A. Uranga, P.-O. Persson, M. Drela, J. Peraire, Implicit Large Eddy Simulation of transition to turbulence at low Reynolds numbers using a Discontinuous Galerkin method, Int. J. Numer. Methods Eng. 87 (1-5) (2011) 232–261. doi:10.1002/nme.3036.
URL `http://dx.doi.org/10.1002/nme.3036`

[14] A. Abbà, L. Bonaventura, M. Nini, M. Restelli, Anisotropic dynamic models for Large Eddy Simulation of compressible flows with a high order DG method, Tech. rep., eprint arXiv.org/abs/1407.6591 (2014).

[15] A. D. Beck, T. Bolemann, D. Flad, H. Frank, G. J. Gassner, F. Hindenlang, C.-D. Munz, High-order discontinuous Galerkin spectral element methods for transitional and turbulent flow simulations, Int. J. Numer. Methods Fluids 76 (8) (2014) 522–548. doi:10.1002/fld.3943.
URL `http://dx.doi.org/10.1002/fld.3943`

[16] C. C. de Wiart, K. Hillewaert, L. Bricteux, G. Winckelmans, Implicit LES of free and wall-bounded turbulent flows based on the discontinuous Galerkin/symmetric interior penalty method, Int. J. Numer. Methods Fluids 78 (6) (2015) 335–354. doi:10.1002/fld.4021.

URL http://dx.doi.org/10.1002/fld.4021

[17] G. Gassner, A. Beck, On the accuracy of high-order discretizations for underresolved turbulence simulations, Theor. Comp. Fluid Dyn. 27 (3-4) (2013) 221–237. doi:10.1007/s00162-011-0253-7.
URL http://dx.doi.org/10.1007/s00162-011-0253-7

[18] F. Bassi, A. Crivellini, D. A. Di Pietro, S. Rebay, An artificial compressibility flux for the discontinuous Galerkin solution of the incompressible Navier-Stokes equations, J. Comput. Phys. 218 (2006) 794–815.

[19] F. Bassi, A. Crivellini, D. A. Di Pietro, S. Rebay, An implicit high-order discontinuous Galerkin method for steady and unsteady incompressible flows, Comput. Fluids 36 (2007) 1529–1546.

[20] F. Bassi, S. Rebay, G. Mariotti, S. Pedinotti, M. Savini, A high-order accurate discontinuous finite element method for inviscid and viscous turbomachinery flows, in: R. Decuypere, G. Dibelius (Eds.), Proceedings of the 2nd European Conference on Turbomachinery Fluid Dynamics and Thermodynamics, Technologisch Instituut, Antwerpen, Belgium, 1997, pp. 99–108.

[21] A. Nigro, A. Ghidoni, S. Rebay, F. Bassi, Modified Extended BDF scheme for the discontinuous Galerkin solution of unsteady compressible flows, Int. J. Numer. Methods Fluids 76 (9) (2014) 549–574. doi:10.1002/fld.3944.
URL http://dx.doi.org/10.1002/fld.3944

[22] A. Nigro, C. De Bartolo, F. Bassi, A. Ghidoni, Up to sixth-order accurate A-stable implicit schemes applied to the discontinuous Galerkin discretized Navier-Stokes equations, J. Comput. Phys. 276 (0) (2014) 136 – 162.

[23] F. Bassi, L. Botti, A. Colombo, A. Ghidoni, F. Massa, Linearly implicit Rosenbrock-type Runge–Kutta schemes applied to the Discontinuous Galerkin solution of compressible and incompressible unsteady flows, Comput. Fluids 118 (2015) 305 – 320. doi:http://dx.doi.org/10.1016/j.compfluid.2015.06.007.

[24] F. Bassi, A. Colombo, C. De Bartolo, N. Franchina, A. Ghidoni, A. Nigro, Investigation of high-order temporal schemes for the discontinuous Galerkin solution of the Navier-Stokes equations, in: 11th World Congress on Computational Mechanics, WCCM 2014, 5th European Conference on Computational Mechanics, ECCM 2014 and 6th European Conference on Computational Fluid Dynamics, ECFD 2014, 2014, pp. 5651–5662.

[25] F. Bassi, L. Botti, A. Colombo, A. Crivellini, N. Franchina, A. Ghidoni, S. Rebay, Very high-order accurate discontinuous Galerkin computation of transonic turbulent flows on aeronautical configurations, in: N. Kroll, H. Bieler, H. Deconinck, V. Couaillier, H. van der Ven, K. Sørensen (Eds.), ADIGMA - A European Initiative on the Development of Adaptive Higher-Order Variational Methods for Aerospace Applications, Vol. 113 of Notes on Numerical Fluid Mechanics and Multidisciplinary Design, Springer Berlin Heidelberg, 2010, pp. 25–38.

[26] F. Bassi, S. Rebay, A high order discontinuous Galerkin method for compressible turbulent flows, in: Discontinuous Galerkin Methods. Theory, Computation and Applications, Vol. 11 of Lecture Notes in Computational Science and Engeneering, Springer-Verlag, 2000, pp. 77–88, *First Internation Symposium on Discontinuous Galerkin Methods*, May 24–26, 1999, Newport, RI, USA.

[27] V. Dolejší, Semi-implicit interior penalty discontinuous Galerkin methods for viscous compressible flows, Commun. Comput. Phys. 4 (2008) 231–274.

[28] G. J. Gassner, F. Lörcher, C.-D. Munz, A discontinuous Galerkin scheme based on a space-time expansion II. Viscous flow equations in multi dimensions, J. Sci. Comput. 34 (2008) 260–286.

[29] L. Botti, Influence of reference-to-physical frame mappings on approximation properties of discontinuous piecewise polynomial spaces, J. Sci. Comput. 52 (3) (2012) 675–703. doi:10.1007/s10915-011-9566-3.

[30] P. Tesini, An *h*-Multigrid Approach for High-Order Discontinuous Galerkin Methods, Ph.D. thesis, University of Bergamo, Bergamo, Italy (January 2008).

[31] F. Bassi, L. Botti, A. Colombo, D. A. Di Pietro, P. Tesini, On the flexibility of agglomeration based physical space discontinuous Galerkin discretizations, J. Comput. Phys. 231 (1) (2012) 45 – 65. doi:10.1016/j.jcp.2011.08.018.

[32] D. A. Di Pietro, A. Ern, Mathematical Aspects of Discontinuous Galerkin Methods, Vol. 69 of Mathématiques et Applications, Springer-Verlag, 2012.

[33] Y.-H. Choi, C. L. Merkle, The application of preconditioning in viscous flows, J. Comput. Phys. 105 (2) (1993) 207 – 223. doi:http://dx.doi.org/10.1006/jcph.1993.1069.

[34] J. M. Weiss, W. A. Smith, Preconditioning applied to variable and constant density flows, AIAA J. 33 (11) (1995) 2050–2057.

[35] F. Bassi, C. De Bartolo, R. Hartmann, A. Nigro, A discontinuous Galerkin method for inviscid low Mach number flows, J. Comput. Phys. 228 (11) (2009) 3996 – 4011. doi:http://dx.doi.org/10.1016/j.jcp.2009.02.021.

[36] G. Hauke, T. J. R. Hughes, A unified approach to compressible and incompressible flows, Comput. Methods Appl. Mech. Engrg. 113 (3–4) (1994) 389 – 395. doi:http://dx.doi.org/10.1016/0045-7825(94)90055-8.

[37] F. Bassi, L. Botti, A. Colombo, A. Crivellini, A. Ghidoni, A. Nigro, S. Rebay, Time Integration in the Discontinuous Galerkin Code MIGALE - Unsteady Problems, in: N. Kroll, C. Hirsch, F. Bassi, C. Johnston, K. Hillewaert (Eds.), IDIHOM: Industrialization of High-Order Methods - A Top-Down Approach, Vol. 128 of Notes on Numerical Fluid Mechanics and Multidisciplinary Design, Springer International Publishing, 2015, pp. 205–230. doi:10.1007/978-3-319-12886-3_11.
URL `http://dx.doi.org/10.1007/978-3-319-12886-3_11`

[38] F. Brezzi, G. Manzini, D. Marini, P. Pietra, A. Russo, Discontinuous Galerkin approximations for elliptic problems, Numer. Meth. Part. D. E. 16 (2000) 365–378.

[39] D. N. Arnold, F. Brezzi, B. Cockburn, L. D. Marini, Unified analysis of discontinuous Galerkin methods for elliptic problems, SIAM J. Numer. Anal. 39 (5) (2002) 1749–1779.

[40] J. J. Gottlieb, C. P. T. Groth, Assessment of Riemann solvers for unsteady one-dimensional inviscid flows of perfect gases, J. Comput. Phys. 78 (1988) 437–458.

[41] D. Hänel, R. Schwane, G. Seider, On the accuracy of upwind schemes for the solution of the Navier–Stokes equations, AIAA Paper 87-1105 (1987).

[42] E. Hairer, G. Wanner, Solving Ordinary Differential Equations II, Stiff and Differential-Algebraic Problems (2nd revised edition), Vol. 14 of Springer Series in Computational Mathematics, Springer Berlin Heidelberg, 1996.

[43] S. Balay, M. F. Adams, J. Brown, P. Brune, K. Buschelman, V. Eijkhout, W. D. Gropp, K. D., M. G. Knepley, L. C.

McInnes, F. Barry, K. R. Smith, H. Zhang, PETSc Web page, `http://www.mcs.anl.gov/petsc` (2014). URL `http://www.mcs.anl.gov/petsc`

[44] A. Crivellini, F. Bassi, An implicit matrix-free discontinuous Galerkin solver for viscous and turbulent aerodynamic simulations, Comput. Fluids 50 (1) (2011) 81–93.

[45] G. S. Iannelli, A. J. Baker, A stiffly-stable implicit Runge-Kutta algorithm for CFD applications, AIAA Paper 88-0416 (1988).

[46] J. Lang, J. Verwer, ROS3P—An accurate third-order Rosenbrock solver designed for parabolic problems, BIT 41 (4) (2001) 731–738.

[47] G. Di Marzo, RODAS5(4) - Méthodes de Rosenbrock d'ordre 5(4) adaptées aux problemes différentiels-algébriques, MSc Mathematics Thesis; Faculty of Science, University of Geneva, Switzerland.

[48] A. Crivellini, V. D'Alessandro, F. Bassi, Assessment of a high-order discontinuous Galerkin method for incompressible three-dimensional Navier-Stokes equations: Benchmark results for the flow past a sphere up to Re=500, Comput. Fluids 86 (0) (2013) 442 – 458. doi:http://dx.doi.org/10.1016/j.compfluid.2013.07.027. URL `http://www.sciencedirect.com/science/article/pii/S004579301300306X`

[49] L. Wei, A. Pollard, Direct numerical simulation of compressible turbulent channel flows using the discontinuous Galerkin method, Comput. Fluids 47 (1) (2011) 85 – 100. doi:http://dx.doi.org/10.1016/j.compfluid.2011.02.015. URL `http://www.sciencedirect.com/science/article/pii/S0045793011000740`

[50] C. Carton de Wiart, K. Hillewaert, M. Duponcheel, G. Winckelmans, Assessment of a discontinuous Galerkin method for the simulation of vortical flows at high Reynolds number, Int. J. Numer. Methods Fluids 74 (7) (2014) 469–493. doi:10.1002/fld.3859.

[51] A. Tomboulides, S. Orszag, Numerical investigastions of the transitional and weak turbulent flow past a sphere, J. of Fluid Mech. 416 (200) 45–73.

[52] J. Wu, G. Faeth, Sphere wakes in still surroundings at intermediate Reynolds numbers, AIAA J. 31 (1993) 1448.

[53] F. Hindenlang, G. J. Gassner, C. Altmann, A. Beck, M. Staudenmaier, C.-D. Munz, Explicit discontinuous Galerkin methods for unsteady problems, Comput. Fluids 61 (0) (2012) 86 – 93.

[54] P. Ploumhans, G. Wincklemans, J. Salmon, A. Leonard, M. Warren, Vortex Methods for Direct Numerical Simulation of Three-Dimensional Bluff Body Flows: Applications to the sphere at Re=300, 500 and 1000, J. of Comp. Phys. 178 (2002) 427–463.

[55] E. K. W. Poon, G. Iaccarino, A. S. H. Ooi, M. Giacobello, Numerical studies of high Reynolds number flow past a stationary and rotating sphere, in: Seventh International Conference on CFD in the Minerals and Process Industries, CSIRO, Melbourne, Australia, 2009.

[56] H. Sakamoto, H. Haniu, A study on vortex shedding from spheres in a uniform flow, J. Fluid Eng. 12 (1990) 386–392.

[57] Z. J. Wang, K. Fidkowski, R. Abgrall, F. Bassi, D. Caraeni, A. Cary, H. Deconinck, R. Hartmann, K. Hillewaert, H. T. Huynh, N. Kroll, G. May, P.-O. Persson, B. van Leer, M. Visbal, High-order CFD methods: Current status

and perspective, Int. J. Numer. Methods Fluids 72 (8) (2013) 811–845.

[58] D. J. Garmann, M. R. Visbal, C3.3: Implicit large eddy-simulations of transitional flow over the SD7003 airfoil using compact finite-differencing and filtering, in: 2nd International Workshop on High-Order CFD Methods, Cologne, Germany, 2013, http://www.dlr.de/as/Portaldata/5/Resources/dokumente/veranstaltungen/2013_05-hiocfd/contrib/C33_Garmann.pdf.

[59] T. Bolemann, A. Beck, D. Flad, H. Frank, V. Mayer, C.-D. Munz, High-Order Discontinuous Galerkin Schemes for Large-Eddy Simulations of Moderate Reynolds Number Flows, in: N. Kroll, C. Hirsch, F. Bassi, C. Johnston, K. Hillewaert (Eds.), IDIHOM: Industrialization of High-Order Methods - A Top-Down Approach, Vol. 128 of Notes on Numerical Fluid Mechanics and Multidisciplinary Design, Springer International Publishing, 2015, pp. 435–456. doi:10.1007/978-3-319-12886-3_20.
URL `http://dx.doi.org/10.1007/978-3-319-12886-3_20`

[60] P. Catalano, R. Tognaccini, RANS analysis of the low-Reynolds number flow around the SD7003 airfoil, Aerospace Science and Technology 15 (8) (2011) 615 – 626.

[61] P. D. Boom, D. W. Zingg, Time-accurate flow simulations using an efficient Newton-Krylov-Schur approach with high-order temporal and spatial discretization, AIAA Paper 2012-0383 (2013).

[62] IDIHOM, Industrialisation of High-Order Methods – A top-down approach, Specific Targeted Research Project supported by European Commission, URL: http://www.dlr.de/as/en/desktopdefault.aspx/tabid-7027/11654_read-27492/.

[63] E. Hairer, S. P. Nørsett, G. Wanner, Solving Ordinary Differential Equations I, Nonstiff Problems (2nd revised edition), Vol. 8 of Springer Series in Computational Mathematics, Springer Berlin Heidelberg, 1993.

[64] J. Dormand, Numerical Methods for Differential Equations: A Computational Approach, Engineering Mathematics, Taylor & Francis, 1996.